Research Article

Assessment of synthesis approaches for tuning the photocatalytic property of ZnO nanoparticles

Parita Basnet[1] · Dhrubajyoti Samanta[1] · T. Inakhunbi Chanu[2] · Jaya Mukherjee[3] · Somenath Chatterjee[1]

Abstract

Tuning the photocatalytic property of zinc oxide (ZnO) nanoparticles (NPs) is timely. Dependence of photocatalysis upon size, morphology and effective surface area of the particles used has led to optimization in various synthesis procedures. The current article addresses to dictate a cost-effective, bio-friendly, modified ease-process for this issue. The synthesis of ZnO NPs with differing photophysical properties, sizes and morphologies, in order to tune its photocatalytic activity, have been extensively studied. Polyethylene glycol as the structure directing agent and different synthesis strategies were adopted. Spectroscopic and microscopic characterization techniques were employed to understand the nature of the as-synthesized samples. Photocatalytic property and photostability of the samples were determined based on experiments performed with common xanthene and azo dyes. Based on analysing the results, certain characteristics, such as smaller particle size, less agglomerated structure, higher surface area and superior lifetime of the photogenerated electrons and holes upon light illumination, were essential for ZnO NPs to act as an efficient photocatalyst.

✉ Somenath Chatterjee, somenath@gmail.com; somenath.c@smit.smu.edu.in | [1]Centre for Material Science and Nanotechnology, Sikkim Manipal Institute of Technology, Sikkim Manipal University, Gangtok, Sikkim, India. [2]Department of Chemistry, Nar Bahadur Bhandari Degree College, Gangtok, Sikkim, India. [3]Laser and Plasma Technology Division, Bhabha Atomic Research Centre, Mumbai, India.
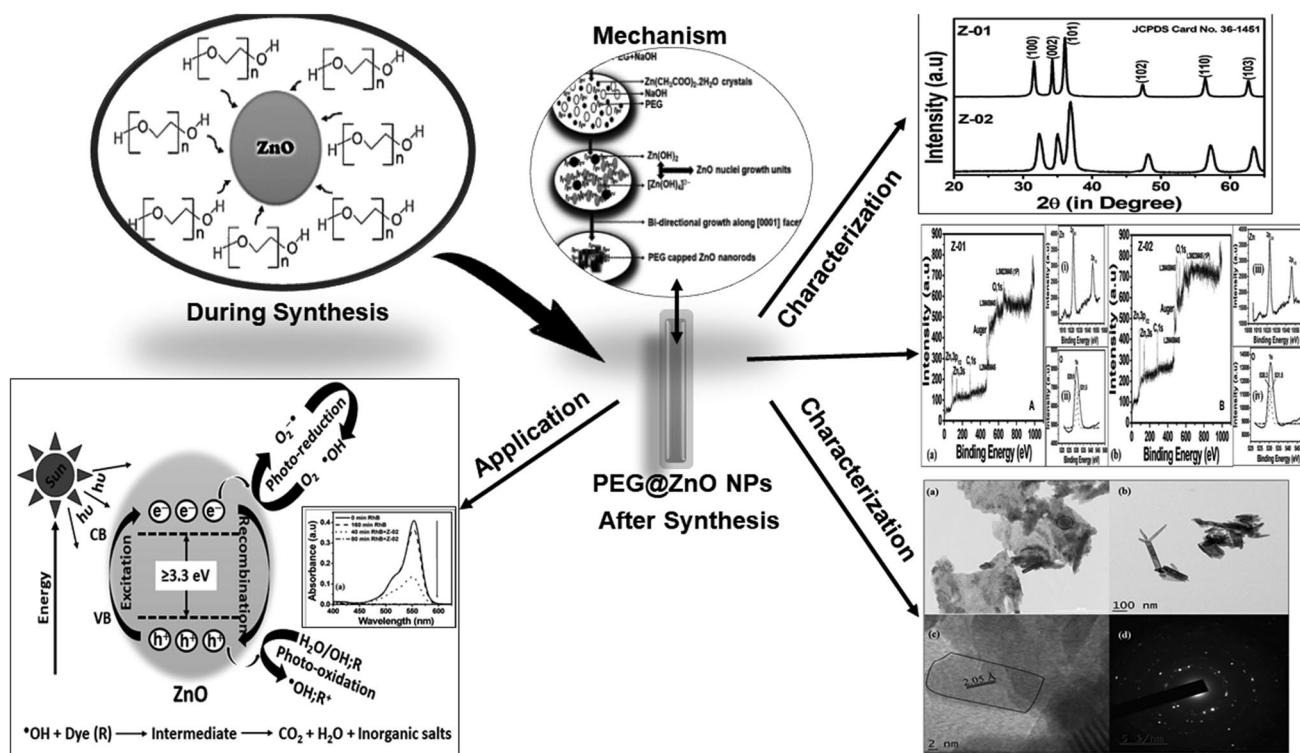
Graphical abstract

1 Introduction

Environmental problems associated to organic wastes disposed in water bodies without proper treatment is a concern and should be accounted using appropriate technologies [1, 2]. Conventional techniques [3], employed for the removal of water pollutants, suffer from several disadvantages like high cost, accumulation of toxic sludge, environmental pollution, and others. An alternative to these techniques is photocatalysis [4] using semiconductor nanomaterials (SNMs), which efficiently degrades organic wastes, such as dyes, drugs, etc. from aqueous media [5–10].

Amongst SNMs, zinc oxide (ZnO) nanoparticles (NPs) have proven to be a highly promising photocatalyst, under ultra-violet (UV) as well as solar light irradiations [1]. ZnO has a direct wide band gap energy of ~ 3.37 eV and has numerous applications due to its nano- and microstructural properties [11–13]. The various applications and multidimensional properties of ZnO NPs have been elaborately discussed by Mishra et al. [14]. The rapid formation and stability of reactive oxidative species (ROS)

in ZnO NPs makes it a highly promising photocatalyst. It has been well established that when the photon energy is higher than the bandgap energy of the photocatalyst, energy absorption takes place which subsequently results into the transfer of electrons from the valence band (VB) of the photocatalyst towards its conduction band (CB), while generating holes in the former [6, 8]. Provided there is less radiative recombination of the as-formed electrons and holes, ROS may be generated in the reaction medium. These ROS then proceeds the reaction further and leads to the breakdown of complex organic molecules, such as dyes [15]. The various defect states present in ZnO NPs [16], such as zinc and oxygen vacancies, may trap either electrons or holes leading to their reduced recombination and thereby, generating higher number of ROS [17].

Alteration of photocatalytic properties may be achieved using different synthesis methods [1, 18, 19], which convey various morphologies of ZnO NPs, such as rods, spheres, tubes and others, with particle size as small as 2–10 nm [20–23]. However, care must be taken about the cost, complexity, feasibility and toxicity of the method opted for synthesis [24]. Ni et al. [22] have demonstrated a cost-effective

and simple hydrothermal process for the synthesis of ZnO nanorods. Likewise, Akir et al. [25] employed an eco-friendly synthesis technique for the fabrication of various morphologies of ZnO NPs. Thus, application specific structure of ZnO NPs may be prepared using various synthesis procedures and parameters.

Particles in the nano-size regime are although beneficial, their stability is a major concern. Modification in the synthesis process using different binders may solve this problem since capping approach enables the control of agglomeration by providing steric hindrance to individual particles belonging to the nano-size regime [26–29]. An example is the work reported by Chakraborty et al. [30], wherein, they have demonstrated the role of Polyethylene glycol (PEG) to control size of the so-formed ZnO NPs (7.7–21 nm). Similarly, the use of various capping agents for structure oriented growth of ZnO NPs have been extensively studied in the previous reports [31, 32]. However, as far as the photocatalytic application is concerned, care must be given such that the capping agents do not passivate the photocatalysts' surface entirely, which would in turn cause less generation of ROS due to hindrance provided at the surface by the binder molecules [33]. Capping approach should be such that the NPs do not agglomerate while keeping the reactive sites available for activity.

Considering these facts, the present study deals with PEG capped synthesis of ZnO NPs. Structural, optical and elemental characterizations were employed for analysing the as-obtained ZnO samples. Common xanthene and azo dyes were used to compare the efficiency of the as-synthesized photocatalysts. As per Authors' perspective, the comparison of different synthesis processes to obtain ZnO NPs in a cost-effective, bio-friendly way and its characterization for material's property understanding, with application towards degradation of organic contaminants (textile by-products) have been systematically presented here. To the best of Author's knowledge, comparison on such synthesis methods, in order to obtain highly efficient photocatalyst for dye degradation, have not yet been reported elsewhere.

2 Experimental details

2.1 Chemicals

All the chemicals were of analytical grade and used without further purifications (99% purity). Zinc acetate dihydrate [$Zn(CH_3COO)_2.2H_2O$], Rhodamine B (RhB), p-Benzoquinone (p-BQ) and Sodium hydroxide (NaOH) were purchased from Loba Chemie. Methylene Blue (MB), Tertiary Butyl Alcohol (t-BA) and Ethylene Diamine Tetra Acetate (EDTA) were purchased from Merck. Polyethylene glycol (PEG) and Methanol were purchased from Rankem. Deionized (DI) water (resistivity: 18.5 MΩ-cm) was used for all analysis.

2.2 Instrumentation

PAN Alytical Spectris technologies PW 3040/60 X-ray diffractometer with Cu Kα$_1$ radiation (λ= 1.54056 Å), working voltage of 40 kV and current of 30 mA was used to analyse the powder X-ray diffraction (XRD) pattern of the samples. High resolution Transmission Electron Microscopy (HRTEM) with LaB$_6$ source and voltage of 200 kV was used for the microstructural analysis. IRAffinity-1S Shimadzu Fourier Transform Infrared Spectrophotometer was employed to obtain the Fourier Transform Infrared Spectroscopic (FTIR) spectrum. UV–Visible (UV–Vis) absorption spectra of all the samples were performed using Shimadzu 1800 UV–Vis spectrophotometer. Surface defects and photophysical studies were analysed using Shimadzu Spectrofluorophotometer (RF-5301 PC) with an excitation wavelength of 320 nm. The intensity of sunlight was measured using a lux-meter (MEXTECH; model no. LX-1010B) with the measured intensity of (1120 X 100) lux for all the photocatalytic experiments.

2.3 Methodology

2.3.1 Synthesis of ZnO NPs

Two different methods were employed for the synthesis of ZnO NPs designated as Z-01 and Z-02. The methods have been described pictorially in Fig. 1.

2.3.2 Photocatalytic studies

The photocatalytic studies were performed based on the methodology and experimental parameters presented in Flowchart 1. Degradation efficiencies of the photocatalysts were calculated from decrease in the concentration of dyes relative to the absorption measurements.

For the assessment of stability, Z-02 sample was used for the degradation of RhB and MB in two consecutive experiments while keeping the same reaction conditions (0.05 g catalyst + 50 ml of RhB and MB solutions: 80 min and 45 min of solar irradiation, respectively). The photocatalyst was recovered by centrifugation after each experiment. To appreciate the role of ROS in the reaction medium towards degradation of the respective dyes, radical scavenging experiments were performed; the procedure used was similar as given above. Based on the degradation efficiency of Z-02 in the presence of radical scavengers, the most active ROS was determined. The amount of Z-02 was taken as 0.05 g for each experiment. The radical scavengers
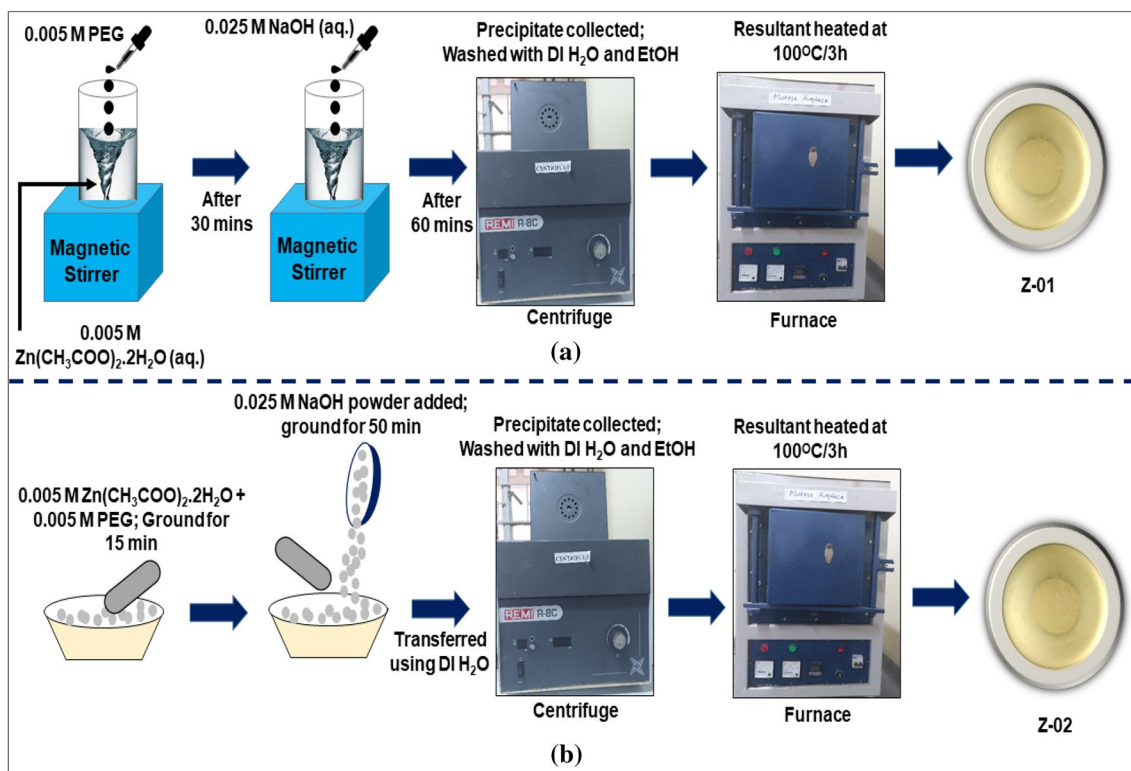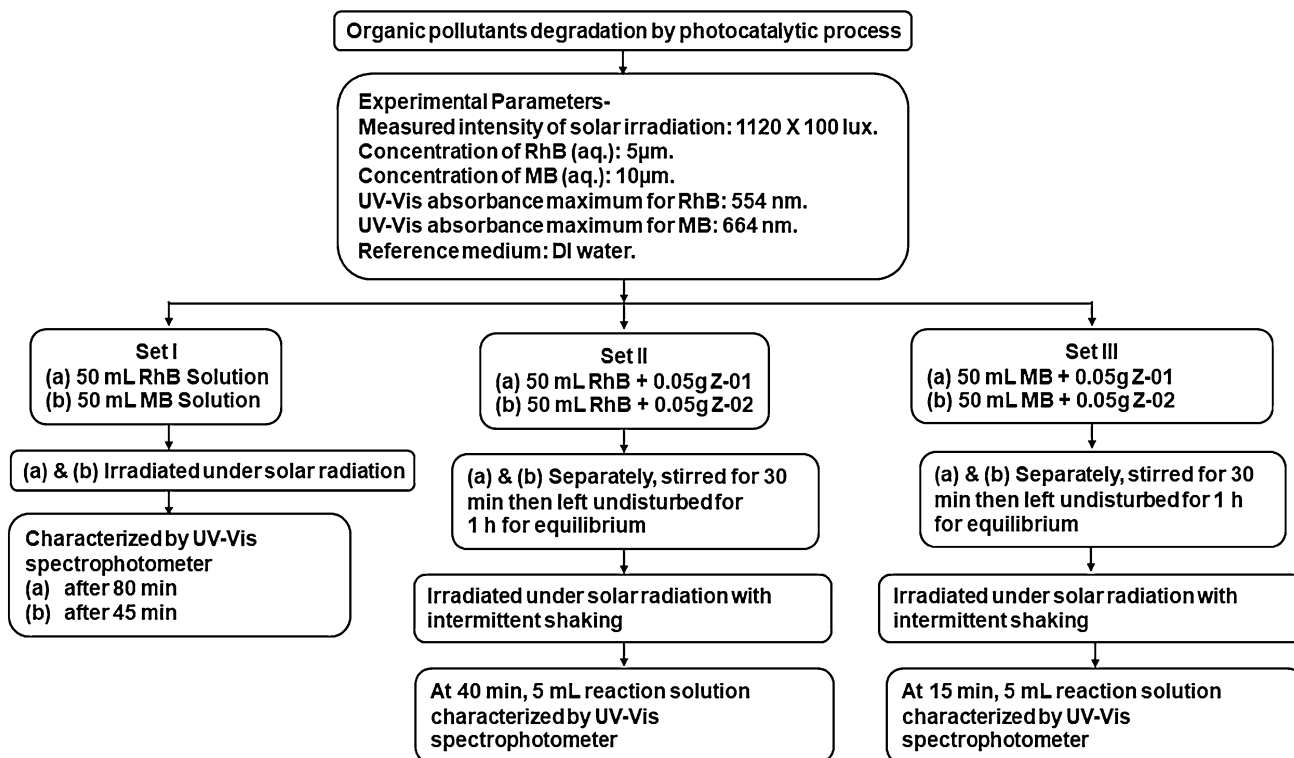
Fig. 1 Pictorial representation of ZnO NPs synthesis for: **a** Z-01, and **b** Z-02

Flowchart 1 Details on the procedure employed to carry out the photocatalytic degradation studies
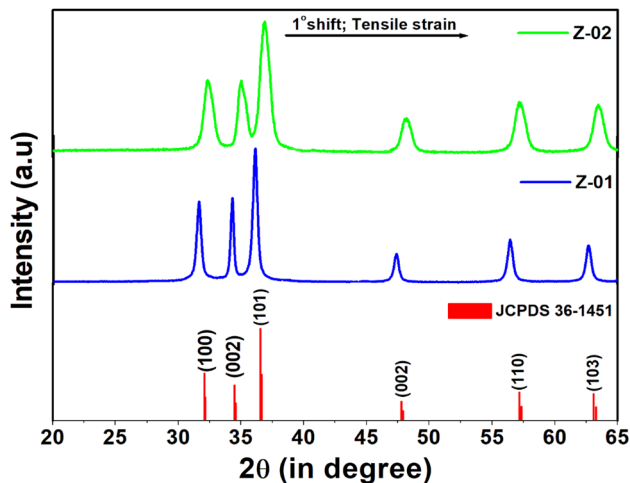
Fig. 2 XRD spectra of ZnO JCPDS 36-1451, Z-01 and Z-02 depicting diffraction planes for wurtzite structure of ZnO with ~ 1° degree shift in the 2θ values for Z-02 w.r.t Z-01 due to microstrain effect (tensile strain)

used were: 15 mg of t-BA as hydroxyl radical (˙OH) scavenger, 15 mg of p-BQ as superoxide radical (O_2^-) scavenger and 15 mg of EDTA for trapping holes (h^+).

3 Results and discussion

3.1 Structural, optical and microstructural characterizations

Figure 2 shows the XRD patterns with wurtzite structures [22] of Z-01 and Z-02 samples (diffraction peaks at 2θ values of 31.59°, 34.23°, and 36.06° for Z-01 and 32.36°, 35.02°, and 36.87° for Z-02). Shifts of approximately 1° in the peak positions for Z-02 was observed. Diffraction peak shifts may be attributed to the presence of microstrain in the sample. In addition, the broadening of diffraction peaks in the XRD pattern is an indication for the presence of microstrain in the respective sample. Microstrain may be induced in the sample due to crystal imperfection and distortion, which may be calculated using Eq. (1) [34].

$$\beta \cos \theta = C\varepsilon \sin \theta + \frac{k\lambda}{D} \tag{1}$$

where, ε is the isotropic microstrain and C is the proportional constant whose value lies between 4 and 5, with C = 4 corresponding to the maximum (upper limit) of strain [35].

Employing Eq. (1), the values of microstrain for Z-01 sample was calculated to be 0.00359 while for Z-02 it was calculated to be 0.27733. From these values of microstrain, negligible effect may be expected in Z-01 whereas,

for Z-02, the value of microstrain is more prominent. In addition, two types of microstrain have been identified, namely, tensile strain and compressive strain depending upon the shift in the XRD peak positions to higher or lower angles, respectively [36]. In this case, as is shown in Fig. 2, shift in the XRD peak positions of Z-02 is toward the higher 2θ values, indicating the presence of tensile strain in the sample. Further, the broadening of XRD peaks represent smaller crystallite size, therefore, formation of smaller crystallites in Z-02 compared to Z-01 may be expected. Using the Debye Scherer equation [6], average crystallite sizes of 21 nm and 11 nm for Z-01 and Z-02, respectively, were calculated. This confirms the presence of smaller crystallites in Z-02. Additionally, the values of lattice (d) spacing for (101) plane, as calculated from Bragg's equation [36], were found to be 2.48 Å for Z-01 and 2.42 Å for Z-02 samples, respectively.

To determine the existence of PEG on the as-synthesized ZnO NPs, FTIR spectra of Z-01 and Z-02 were recorded in the scanning range of 600–3400 cm^{-1} and are presented in Fig. 3. The spectra of both Z-01 and Z-02 show similar band positions with slight difference in their transmittance intensity, indicating strong and weak adsorption of PEG on the surface of Z-02 and Z-01, respectively. The prominent FTIR band positions [37–40] are marked in Fig. 3. The band at 1387.8 cm^{-1}, assigned to the C–O–H bending vibration of adsorbed PEG on ZnO surface [40] and the band appearing at 776 cm^{-1}, attributed to the bending of long polymeric chain [40], confirms the successful adsorption of PEG on both the samples.

The UV–Vis absorption spectra for Z-01 and Z-02, measured by ultra-sonically dispersing the samples in DI water, are shown in Fig. 4a. The given spectra are corrected for water contribution. The representative absorption peaks are slightly blue shifted with respect to the absorption peak of bulk ZnO appearing at around 380 nm [41]. These shifts may be attributed to the presence of smaller particles in the respective samples. The occurrence of strong narrow absorption peaks may be ascribed to the intrinsic band gap absorption of ZnO NPs due to electron transitions from the valence band of O_{2p} to the conduction band of Zn_{3d}. Moreover, the existence of sharp peak indicates that the particles are smaller in size with a narrow particle size distribution [42, 43]. From the spectra curves, band-edge absorption beginning at 1000 nm wavelength was observed, suggesting that more absorption states or defect energy bands exist in the samples [44]. Figure 4b shows the estimation of optical band gap energies (E_g) for Z-01 and Z-02 samples calculated using the Tauc equation (Eq. 2),

$$E_g = h\upsilon - \left(\frac{\alpha h \upsilon}{B}\right)^2, \tag{2}$$

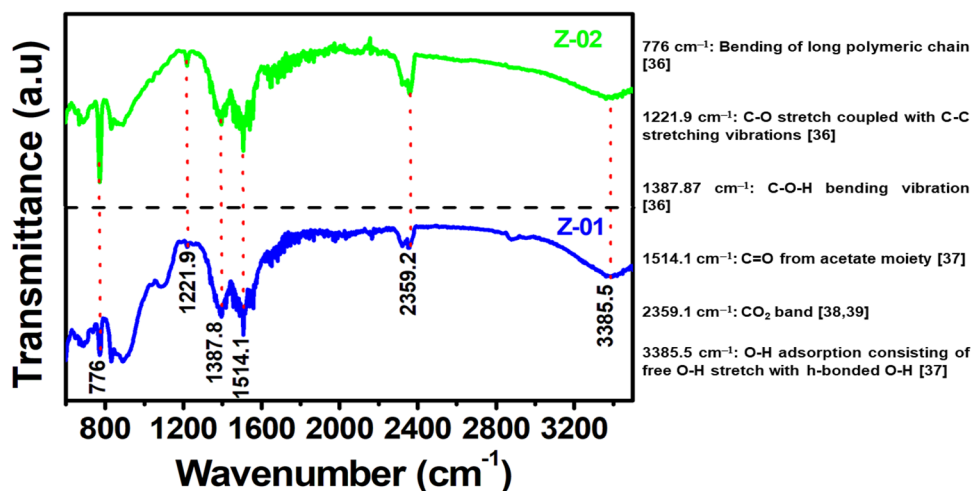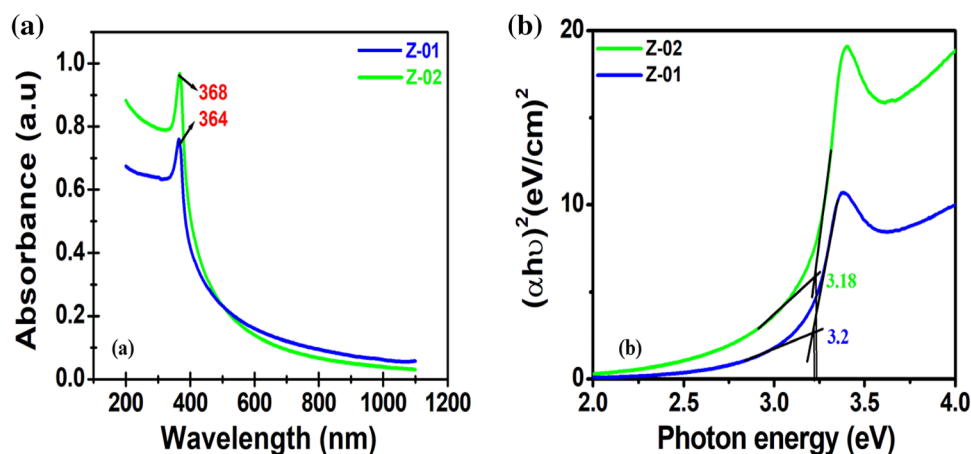**Fig. 3** FTIR spectra of as-synthesized ZnO samples with corresponding values and bonding information

Fig. 4 **a** UV–Vis absorption spectra, and **b** Tauc plot of Z-01 and Z-02 samples, respectively

where α is the absorption co-efficient, hυ is the photon energy, and B is a proportionality constant.

The band gap energy calculated from the plot of $(αhυ)^2$ versus hυ (shown in Fig. 4b) by the extrapolation of linear portion of the curve to energy axis for as-synthesized Z-01 and Z-02 are 3.2 eV and 3.18 eV, respectively. These values are lower than the band gap of bulk ZnO (3.37 eV). It has been reported that blue-shift in the absorption peak arises when size of the particle decreases giving rise to larger band gap energy. However, in this case for ZnO NPs, band gap energy smaller than that of bulk ZnO has been observed [45] which may be due to the existence of valence-band donor level overlap by the surface states [46] or the insertion of defect levels within the band gap [47].

To understand the photophysical phenomenon of the as-synthesised ZnO NPs, Photoluminescence (PL) studies were carried out with excitation wavelength of 320 nm. It has been well established that the UV-range emission, called radioactive recombination, occurs due to the recombination of excitons, while, the visible range emission, called non-radiative recombination, corresponds to the recombination of electrons in a deep defect level or a shallow surface defect level with holes present in the VB [48].

The PL spectra of Z-01 and Z-02 samples are presented in Fig. 5a, wherein, the prominent peaks in PL emission are marked. The non-radiative recombination is pre-dominant in both the cases, indicating the occurrence of defect states in the samples which resulted in lowering of the optical bandgap energy. The sharp Lorentzian peak centred at around 642 nm represents the orange-red emission, which exists due to the transition of electrons from CB to oxygen interstitials region [49]. Additionally, the intensity of orange-red emission is stronger for Z-01 as compared to Z-02. This indicates that relatively more oxygen interstitials are present in Z-01 than Z-02 [50]. A small hump in the green emission region observed in both the samples represent recombination of a shallowly trapped electron with a deeply trapped hole at valence band of Zn and oxygen interstitials [51].

Fig. 5 **a** PL spectra of Z-01 and Z-02 showing various emission states, and **b** magnified view of blue-emission region
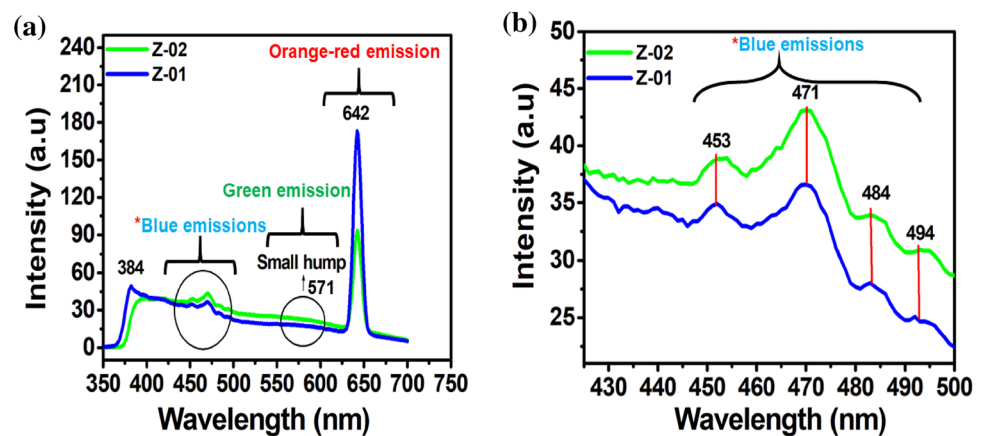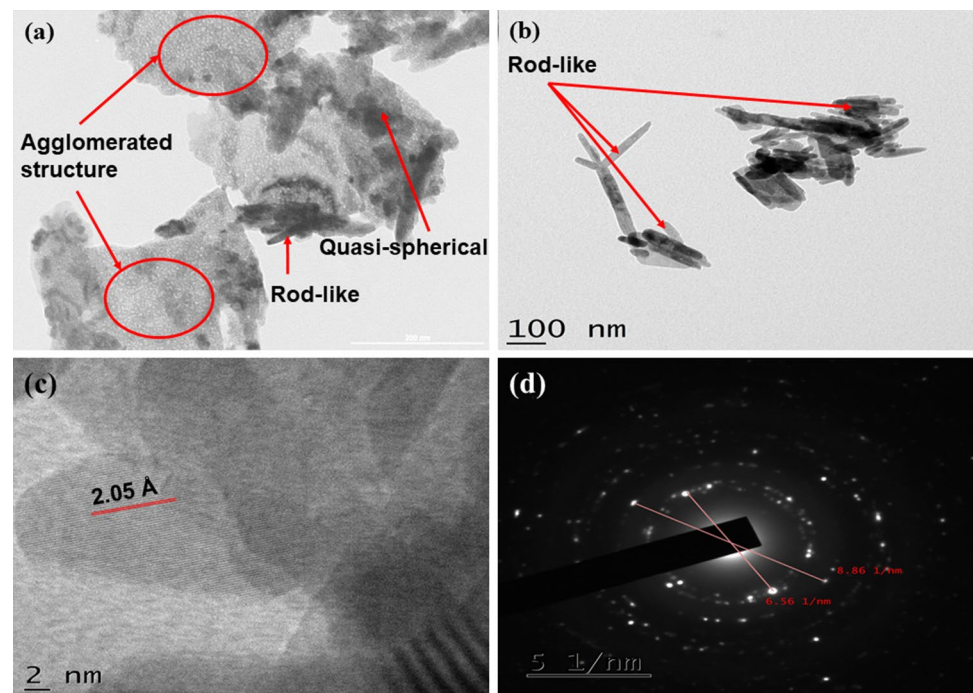

Fig. 6 TEM images of **a** Z-01, and **b** Z-02, **c** HRTEM image displaying the lattice fringes of Z-02, and **d** SAED pattern of Z-02, respectively

The blue-emissions occurring at 453 nm and 471 nm, as shown in Fig. 5b, corresponds to the singly ionised Zn vacancies [52]. This figure shows the existence of two blue-green emission bands (or weak green emission) at 484 nm and 494 nm, which may be attributed to the transition between oxygen vacancy and oxygen interstitial defects [50]. The presence of such multiple peaks in the visible region is typical for ZnO NPs [53]. The near band gap excitonic emission occurring in the UV-region at ~384 nm may be ascribed to the radiative recombination between the excitons (i.e. electrons in the conduction band and holes in the valence band) [54]. Hence, the as-synthesized ZnO NPs (both Z-01 and Z-02) have surface defects, as supported by the UV–Vis spectroscopic analysis. Moreover, the relatively smaller orange-red emission band and weak near

band-edge emission in case of Z-02 than Z-01, suggests that recombination of electron and hole pairs in Z-02 is limited as compared to Z-01.

To determine the microstructures of Z-01 and Z-02 samples, TEM characterizations were performed as depicted in Fig. 6a, b which represents the TEM images of Z-01 and Z-02, respectively. As may be observed from Fig. 6a, particles in Z-01 are highly agglomerated. This means that the functionality of PEG in Z-01 was not sufficient for controlling agglomeration. As a result, determination of particle size in this sample could not be carried out. However, in case of Z-02, the formation of ZnO nanorods is quite visible, which may be observed in Fig. 6b, wherein, PEG played the role of structure directing agent. The difference in the functionality of PEG in these samples may be attributed
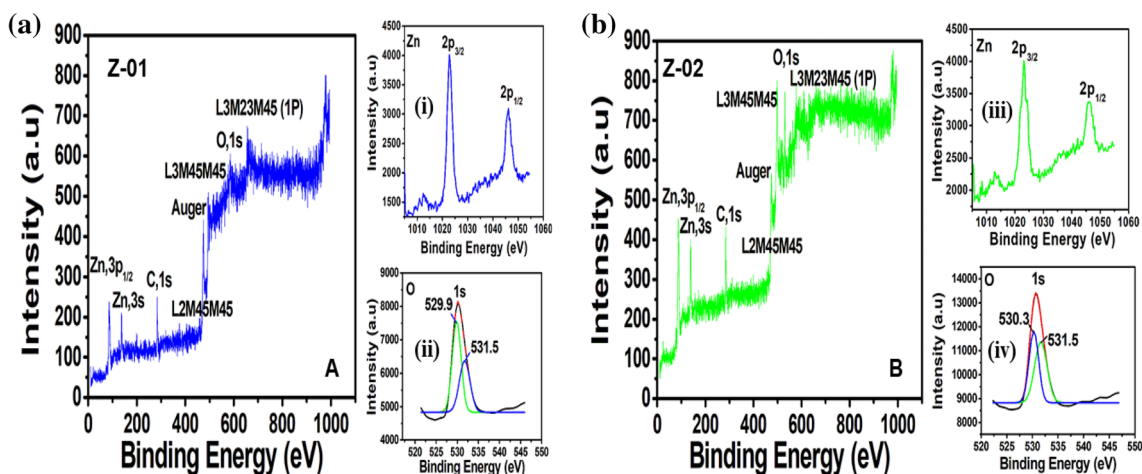
Fig. 7 XPS spectra of **a** Z-01, and **b** Z-02, where, (A) XPS wide survey spectra of Z-01, (B) XPS wide survey spectra of Z-02, (i) Zn 2p for Z-01, (ii) deconvoluted spectrum of O 1s for Z-01, (iii) Zn 2p for Z-02, and (iv) deconvoluted spectrum O 1s for Z-02, respectively

to the different mechanisms of ZnO NPs synthesis. The average particle size in Z-02 ranges from 25–60 nm. Figure 6c represents the High resolution TEM (HRTEM) image of Z-02. The value of d-spacing is calculated as 0.205 nm (2.05 Å) for (101) plane of Z-02, which is consistent with the value obtained from the XRD analysis (2.42 Å). Figure 6d represents the selected area electron diffraction (SAED) pattern of Z-02 through which, nature of the sample may be identified. Herein, the SAED pattern confirms the polycrystalline nature of Z-02.

The elemental composition and oxidation states on the surface and sub-surface of the as-synthesized samples were investigated through XPS analysis. Figure 7a, b shows the XPS spectra of Z-01 and Z-02, respectively. The wide survey scan of Z-01 is depicted in fig.: A, with figs. (i) and (ii) representing the Zn 2p core levels and O 1s level, respectively. The appearance of two strong peaks at 1022.90 eV [55, 56] and 1045.9 eV [57] are evident from fig.: (i), which corresponds to the binding energy core levels of Zn $2p_{3/2}$ and Zn $2p_{1/2}$, respectively. The spin-orbital energy difference of 23 eV indicated that Zn is present in the sample as Zn^{2+} [45]. XPS spectra of O 1s of Z-01, as shown in fig.: (ii), has been deconvoluted into two peaks (Gaussian fitting) at 529.9 eV and 531.5 eV, respectively. The peak at the lower binding energy (529.9 eV) is accredited to the anionic (2−) states of oxygen in the wurtzite geometry of Zn^{2+} ion array [58], while the peak at the higher binding energy (531.5 eV) corresponds to bulk oxygen (O 1s) involvement from the adsorbed oxygen of the polymer used (PEG) [59, 60]. Similarly, fig.: B shows the wide survey scan of Z-02, while figs.: (iii) and (iv) represent the Zn 2p and O 1s levels, respectively. Similar to Z-01, two strong Zn peaks appeared at binding energy values of 1023.14 eV [61, 62] and 1046.14 eV [61], respectively for

Z-02, corresponding to Zn $2p_{3/2}$ and Zn $2p_{1/2}$ sub-shells with the spin-orbital energy difference of 23 eV, indicating the presence of Zn^{2+} ions. The deconvoluted peaks of oxygen appearing at 530.3 eV corresponds to the presence of O_2^- in Z-02 [63, 64].

3.2 Mechanism of ZnO nanorods formation

The growth unit of ZnO nanocrystal has usually been described to be either $Zn(OH)_2$ or $[Zn(OH)_4]^{2-}$ species depending upon the pH of the reaction [65]. Based on Literature [66, 67], in strong alkaline medium, the latter acts as the dominant species for ZnO nuclei formation. Here, as the concentration of OH⁻ ion is relatively high than Zn^{2+} ions ($M_{Zn}^{2+}:M_{OH}^- = 1:5$), ZnO nuclei must have been predominantly formed from the dehydration of $[Zn(OH)_4]^{2-}$ species. The reaction involved the mixing of zinc salt with NaOH and PEG, which led to the formation of Zn ion (Zn^{2+}). This Zn^{2+} then reacted with hydroxyl ion to form $[Zn(OH)_4]^{2-}$ under alkaline condition. The nucleation process guided the bi-directional growth of [0001] (positive) and [0001] negative faces of the crystal because of dipole interaction. Therefore, the formation of $[Zn(OH)_4]^{2-}$ species directed the growth of rod-like ZnO NPs, mainly bounded by hexagonal prism [0110]. Moreover, in the crystallisation process, a possible interaction exists between the precursor and the polymer (PEG), wherein, PEG not only serves as a growth director but also acts as a binder to prevent agglomeration of the particles. Various types of developed complexes of $[Zn(OH)_4]^{2-}$ get adsorbed on newly formed ZnO nuclei, leading to the elongation of c-axis. This then, extend predominantly towards the [0001] facet, causing an increase in the number of elongated ZnO particles.

A schematic mechanism depicting the growth of ZnO nanorods has been provided in Fig. 8.

3.3 Photocatalytic studies

A xanthene dye, RhB and an azo dye, MB were selected for evaluating the photocatalytic activities of the as-synthesized Z-01 and Z-02 under solar irradiation. The temporal adsorption spectral changes of the dye solutions, taking place during sunlight illumination, have been illustrated in Figs. 9 and 10 for RhB and MB, respectively. For comparison, photolysis processes were also conducted for these
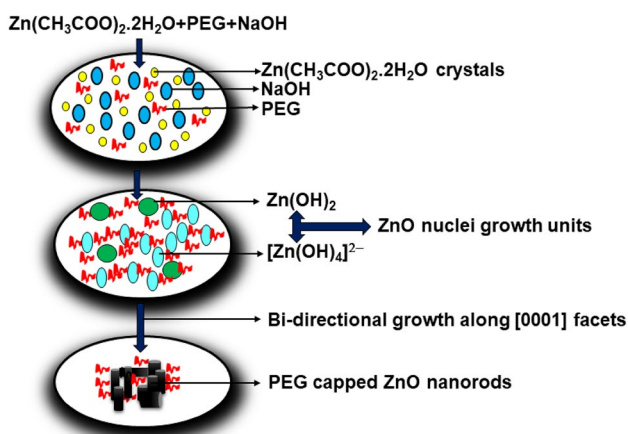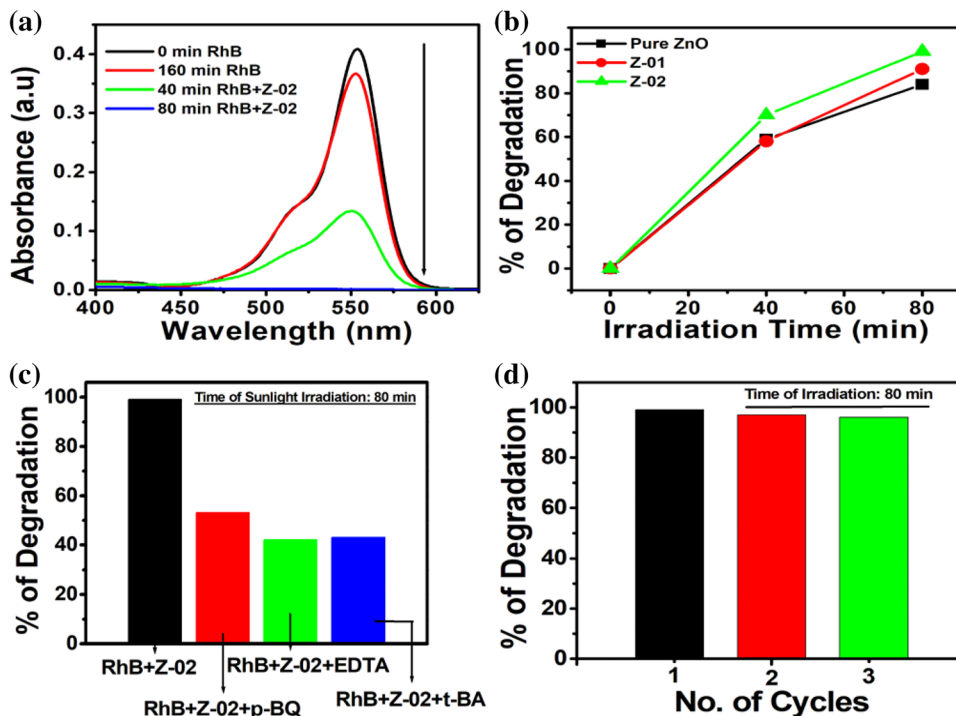

Fig. 8 Schematic representation for the possible formation mechanism of ZnO nanorods

dye solutions under identical conditions. It may be seen in Fig. 9a that after 160 min of photolysis, negligible reduction in the intensity of RhB peaks appearing at 554 nm and 512 nm, respectively, indicating that RhB solution is fairly stable towards solar irradiation. The absorbance maximum of RhB decreased sharply within 40 min when the aqueous solution of RhB mixed with Z-02 sample was exposed under solar irradiation. The absorption maximum of RhB further decreased to reach a minimum (~ 0), indicating that the chromophoric group as well as the dye dimer of RhB molecule have broken down. Thus, the presence of photocatalyst is essential to accelerate the degradation process. In terms of exhibiting efficient photocatalytic activity, bulk ZnO is also a potential candidate [68]. A comparison based on the photocatalytic effect of Z-01, Z-02 as well as bulk ZnO towards RhB degradation has been studied. From Fig. 9b, it may be observed that, over the same period of time (80 min), bulk ZnO offered 84% of degradation efficiency, while the photodegradation efficiencies of both the capped samples (Z-01 and Z-02) were above 90%, confirming the activity of NPs towards faster dye degradation.

The photocatalytic degradation of dyes is favoured by the activity of ROS in the reaction medium [69–71]. These ROS, particularly, hydroxyl radicals (OH·), superoxide radicals (O_2^-) and holes (h^+), undergo redox-reactions with the adsorbed dye molecules to form simple inorganic compounds. Results of the radical scavenging experiments are shown in Fig. 9c. In the absence of scavengers, maximum degradation occurred, while in the presence of

Fig. 9 **a** UV–Vis absorption spectra depicting decrease in the absorbance maximum of RhB with respect to time of irradiation in the presence of Z-02, **b** percentage of Photocatalytic degradation of RhB by Z-01, Z-02 and bulk ZnO, **c** role of reactive oxidative species (ROS) towards RhB photocatalytic degradation, and **d** reusability of Z-02 for RhB degradation, respectively

Fig. 10 **a** UV–Vis absorption spectra of MB degradation by Z-01 under sunlight exposure, **b** UV–Vis absorption spectra of MB degradation by Z-02 under sunlight illumination, **c** percentage of MB degradation by Z-01 and Z-02, and **d** reusability of Z-02 towards MB degradation, respectively
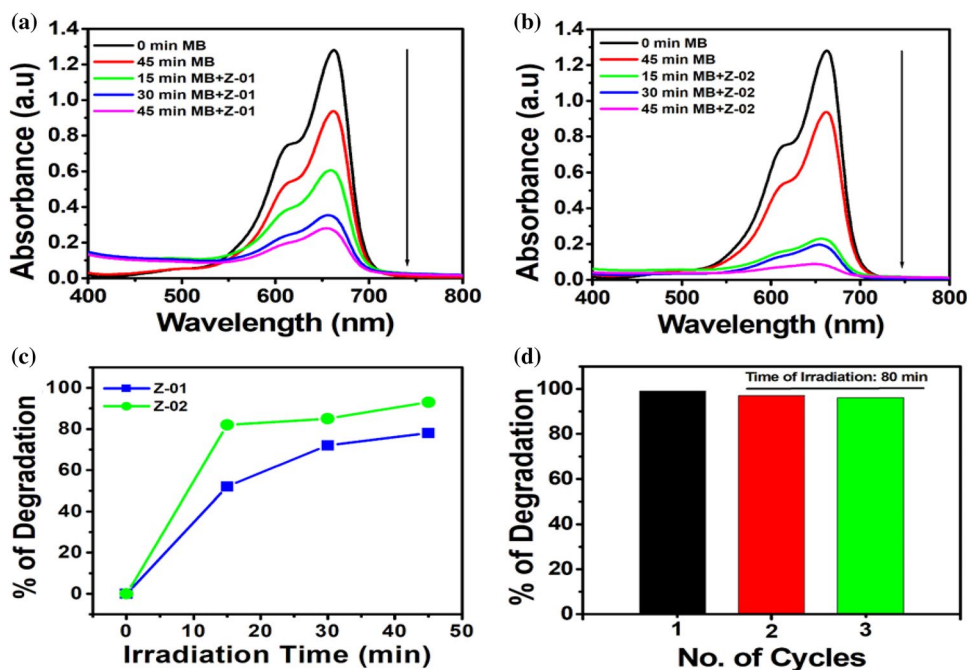

different radical scavengers, the percentage of degradation decreased significantly. This indicates that all ROS are important for efficient photocatalytic degradation of dyes. Least photodegradation occurred with EDTA and t-BA, indicating that the radicals complimentary to these scavengers, i.e. h^+ and $OH^.$, respectively, were the species mostly responsible for degrading RhB compared to O_2^-. Another important aspect of a good photocatalyst is its stability against multiple usage. Figure 9d represents the efficiency of Z-02 towards RhB degradation over 3 consecutive cycles which is identical, indicating that the sample Z-02 is fairly stable. Therefore, Z-02 may prove to be a beneficial candidate for industrial applications.

Photocatalytic degradation of MB was performed to test whether the as-synthesized samples were effective towards an azo dye or not. MB shows a strong absorbance band at around 664 nm, which represents the chromophoric group and a shoulder peak at around 612 nm, corresponding to the dye dimer. Figure 10a shows the decrease in absorbance spectra of MB dye due to the effect of photocatalytic reaction in the presence of Z-01. As may be observed, MB is a stable dye under sunlight exposure. However, this photolysis reaction may be accelerated through the addition of ZnO photocatalyst, which drastically accelerates the reaction process. Figure 10b represents the decrease in absorption maxima of MB due to Z-02 addition. On comparing Fig. 10a, b, Z-02 has exhibited relatively better photocatalytic activity than Z-01, which may be attributed to its smaller particle size and limited electron-hole pair recombination. From Fig. 10c, the percentage of MB degradation by Z-01 and Z-02 were

calculated to be 77% and 95% in 45 min, respectively. This indicates that in case of MB dye also, Z-02 is more competent than Z-01. In terms of stability, Z-02 confirms that it is a stable photocatalyst with negligible loss in degradation percentage over three consecutive cycles, as depicted in Fig. 10d.

An important point is the fact that MB degradation occurred much faster than RhB degradation. This may be due to the negative zeta potential of ZnO which makes the adsorption of cationic dye, MB, more favourable than RhB [72]. The better photocatalytic activity of Z-02 as compared to Z-01 may be due to the smaller particle size, fine structure (nanorod) with relatively lesser agglomeration and higher surface defects in the sample. Further, the pathway of dye degradation follows two basic mechanisms, one is by *N*-demethylation and the other through the destruction of conjugated structure [6]. Here, the degradation is probably due to the destruction of conjugated structure [6]. The mechanism of RhB degradation may be explained according to Scheme 1. Photoexcitation of electrons take place in ZnO NPs when exposed to solar radiation. These electrons reduce adsorbed oxygen molecules into superoxide radicals (O_2^-) and the water molecules to form hydroxide ($HO^.$) or hydroperoxyl radicals ($HO_2^.$). Additionally, holes in the valence band oxidise the adsorbed water or OH^- and produce $^.OH$. These ROS then degrade dye molecules (represented by 'R' in Scheme 1) into simple inorganic molecules [73].
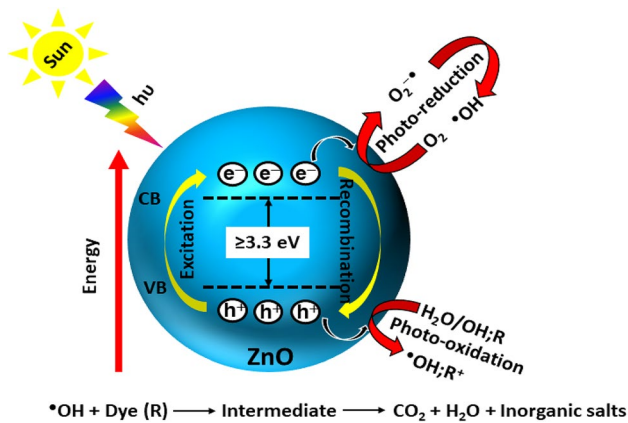
Scheme 1 Schematic for the reaction mechanism for the photocatalytic degradation of the dye molecules

4 Conclusions

This work reports a successful tuning of the photocatalytic properties of ZnO NPs using different synthesis methods. On the basis of obtained results, smaller crystallite size, more number of defect states and nanorod structure of Z-02 proved to be important parameters contributing towards faster photodegradation with 99% of RhB degradation in 120 min and 95% of MB degradation in 45 min. Higher adsorption capability of MB over RhB, led to its faster degradation than RhB. Moreover, due to the larger surface area of the particles belonging to the nano-size regime, enhanced photodegradation was observed with Z-01 and Z-02 compared to bulk ZnO.

Compliance with ethical standards

Conflict of interest The Authors declare that they have no conflict of interest.

References

1. Basnet P, Chanu TI, Samanta D, Chatterjee S (2018) A review on bio-synthesized zinc oxide nanoparticles using plant extracts as reductants and stabilizing agents. J Photochem Photobiol B Biol 183:201–221. https://doi.org/10.1016/j.jphotobiol.2018.04.036
2. Baruah S, Jaisai M, Imani R, Nazhad MM, Dutta J (2010) Photocatalytic paper using zinc oxide nanorods. Sci Technol Adv Mater 11:15–20. https://doi.org/10.1088/1468-6996/11/5/055002
3. Meziti C, Boukerroui A (2012) Removal of a basic textile dye from aqueous solution by adsorption on regenerated clay. Proc Eng 33:303–312. https://doi.org/10.1016/j.proeng.2012.01.1208
4. Park SJ, Das GS, Schütt F, Adelung R, Mishra YK, Tripathi KM, Kim TY (2019) Visible-light photocatalysis by carbon-nano-onion-functionalized ZnO tetrapods: degradation of 2,4-dinitrophenol and a plant-model-based ecological assessment. NPG Asia Mater. https://doi.org/10.1038/s41427-019-0107-0
5. Wu Q, Chen X, Zhang P, Han Y, Chen X, Yan Y, Li S (2008) Amino acid-assisted synthesis of ZnO hierarchical architectures and their novel photocatalytic activities. Cryst Growth Des 8:3010–3018. https://doi.org/10.1021/cg800126r
6. Chanu TI, Samanta D, Tiwari A, Chatterjee S (2016) Effect of reaction parameters on photoluminescence and photocatalytic activity of zinc sulfide nanosphere synthesized by hydrothermal route. Appl Surf Sci 391:548–556. https://doi.org/10.1016/j.apsusc.2016.05.045
7. Samanta D, Chanu TI, Basnet P, Chatterjee S (2018) Organic dye degradation under solar irradiation by hydrothermally synthesized ZnS nanospheres. J Mater Eng Perform. https://doi.org/10.1007/s11665-018-3214-0
8. Samanta D, Chanu TI, Chatterjee S (2017) Citrus limetta juice as capping agent in hydrothermal synthesis of ZnS nanosphere for photocatalytic activity. Mater Res Bull 88:85–90. https://doi.org/10.1016/j.materresbull.2016.11.019
9. Chanu TI, Samanta D, Tiwari A, Chatterjee S (2017) Effect of reaction parameters on morphology and photoluminescence of intrinsic and Mn-doped ZnS microspheres synthesized by hydrothermal method. J Mater Eng Perform. https://doi.org/10.1007/s11665-017-3064-1
10. Fei BJ, Cui Y, Yan X, Qi W, Yang Y, Wang K, He Q, Li J (2008) Controlled preparation of MnO₂ hierarchical hollow nanostructures and their application in water treatment. Adv Mater 20:452–456. https://doi.org/10.1002/adma.200701231
11. Nandi SK, Chatterjee S, Samanta SK, Bose PK, Maiti CK (2007) Electrical characterization of low temperature deposited oxide films on ZnO/n-Si substrate. Bull Mater Sci 26:693–697. https://doi.org/10.1007/bf02706765
12. Chatterjee S, Nandi SK, Maikap S, Samanta SK, Maiti CK (2003) Electrical properties of deposited ZrO2 films on ZnO/n-Si substrates. Semicond Sci Technol 18:92–96. https://doi.org/10.1088/0268-1242/18/2/305
13. Gröttrup J, Schütt F, Smazna D, Lupan O, Adelung R, Mishra YK (2017) Porous ceramics based on hybrid inorganic tetrapodal networks for efficient photocatalysis and water purification. Ceram Int 43:14915–14922. https://doi.org/10.1016/j.ceramint.2017.08.008
14. Mishra YK, Adelung R (2018) ZnO tetrapod materials for functional applications. Mater Today. https://doi.org/10.1016/j.mattod.2017.11.003
15. Kou J, Lu C, Wang J, Chen Y, Xu Z, Varma RS (2017) Selectivity enhancement in heterogeneous photocatalytic transformations. Chem Rev. https://doi.org/10.1021/acs.chemrev.6b00396
16. Smazna D, Rodrigues J, Shree S, Postica V, Neubüser G, Martins AF, Ben Sedrine N, Jena NK, Siebert L, Schütt F, Lupan O, Ahuja R, Correia MR, Monteiro T, Kienle L, Yang Y, Adelung R, Mishra YK

(2018) Buckminsterfullerene hybridized zinc oxide tetrapods: defects and charge transfer induced optical and electrical response. Nanoscale 10:10050–10062. https://doi.org/10.1039/c8nr01504j

17. Maji TK, Bagchi D, Kar P, Karmakar D, Pal SK (2017) Enhanced charge separation through modulation of defect-state in wide band-gap semiconductor for potential photocatalysis application: ultrafast spectroscopy and computational studies. J Photochem Photobiol A Chem 332:391–398. https://doi.org/10.1016/j.jphotochem.2016.09.017

18. Mädler L, Stark WJ, Pratsinis SE (2002) Rapid synthesis of stable ZnO quantum dots. J Appl Phys 92(11):6537–6540. https://doi.org/10.1063/1.1518132

19. Zhu Y, Zhou Y (2008) Preparation of pure ZnO nanoparticles by a simple solid-state reaction method. Appl Phys A Mater Sci Process 92:275–278. https://doi.org/10.1007/s00339-008-4533-z

20. Pung S, Lee W, Aziz A (2012) Kinetic study of organic dye degradation using ZnO particles with different morphologies as a photocatalyst. Int J Inorg Chem 2012:1–9. https://doi.org/10.1155/2012/608183

21. Duan J, Huang X, Wang E (2006) PEG-assisted synthesis of ZnO nanotubes. Mater Lett 60:1918–1921. https://doi.org/10.1016/j.matlet.2005.12.052

22. Ni YH, Wei XW, Hong JM, Ye Y (2005) Hydrothermal preparation and optical properties of ZnO nanorods. Mater Sci Eng B Solid-State Mater Adv Technol 121:42–47. https://doi.org/10.1016/j.mseb.2005.02.065

23. Huang W, Bai D, Li L, Wei H, Shi Z, Cheng H, Li Y (2015) The synthesis of ultrasmall ZnO@PEG nanoparticles and its fluorescence properties. J Sol-Gel Sci Technol 74:718–725. https://doi.org/10.1007/s10971-015-3653-0

24. Demille TB, Hughes RA, Preston AS, Adelung R, Mishra YK, Neretina S (2018) Light-mediated growth of noble metal nanostructures (Au, Ag, Cu, Pt, Pd, Ru, Ir, Rh) from micro- and nanoscale ZnO tetrapodal backbones. Front Chem 6:1–8. https://doi.org/10.3389/fchem.2018.00411

25. Akir S, Barras A, Coffinier Y, Bououdina M, Boukherroub R, Omrani AD (2016) Erratum: Corrigendum to 'Eco-friendly synthesis of ZnO nanoparticles with different morphologies and their visible light photocatalytic performance for the degradation of Rhodamine B'. Ceram Int 42:10259–10265. https://doi.org/10.1016/j.ceramint.2016; Ceram Int 42:16437. https://doi.org/10.1016/j.ceramint.2016.06.187

26. Tanna JA, Chaudhary RG, Juneja HD, Gandhare NV, Rai AR (2015) Histidine-capped ZnO nanoparticles: an efficient synthesis. Spectral Charact Eff Antibact Activity Bionanosci 5:123–134. https://doi.org/10.1007/s12668-015-0170-0

27. Raja K, Ramesh PS, Geetha D, Kokila T, Sathiyapriya R (2015) Synthesis of structural and optical characterization of surfactant capped ZnO nanocrystalline. Spectrochim Acta Part A Mol Biomol Spectrosc 136:155–161. https://doi.org/10.1016/j.saa.2014.08.092

28. Ramimoghadam D, Bin Hussein MZ, Taufiq-Yap YH (2012) The effect of sodium dodecyl sulfate (SDS) and cetyltrimethylammonium bromide (CTAB) on the properties of ZnO synthesized by hydrothermal method. Int J Mol Sci 13:13275–13293. https://doi.org/10.3390/ijms131013275

29. Zhang L, Jiang Y, Ding Y, Povey M, York D (2007) Investigation into the antibacterial behaviour of suspensions of ZnO nanoparticles (ZnO nanofluids). J. Nanoparticle Res 9:479–489. https://doi.org/10.1007/s11051-006-9150-1

30. Chakraborty S, Kumbhakar P (2014) Effect of polyethylene glycol on the particle size and photoluminescence emissions characteristics of chemically synthesized ZnO nanoparticles. Opt Commun 318:61–66. https://doi.org/10.1016/j.optcom.2013.12.036

31. Singh AK, Viswanath V, Janu VC (2009) Synthesis, effect of capping agents, structural, optical and photoluminescence properties of ZnO nanoparticles. J Lumin 129:874–878. https://doi.org/10.1016/j.jlumin.2009.03.027

32. Javed R, Usman M, Tabassum S, Zia M (2016) Effect of capping agents: structural, optical and biological properties of ZnO nanoparticles. Appl Surf Sci 386:319–326. https://doi.org/10.1016/j.apsusc.2016.06.042

33. Campisi S, Schiavoni M, Chan-Thaw C, Villa A (2016) Untangling the role of the capping agent in nanocatalysis: recent advances and perspectives. Catalysts 6:185. https://doi.org/10.3390/catal6120185

34. Krishna AG, Ravikumar RVSSN, Kumar TV, Ephraim SD, Ranjith B, Pranoy M, Dola S (2016) Investigation and comparison of optical and raman bands of mechanically synthesised MoO3 nano powders. Mater Today Proc 3:54–63. https://doi.org/10.1016/j.matpr.2016.01.121

35. Bindu P, Thomas S (2014) Estimation of lattice strain in ZnO nanoparticles: X-ray peak profile analysis. J Theor Appl Phys 8:123–134. https://doi.org/10.1007/s40094-014-0141-9

36. Thandavan TMK, Gani SMA, Wong CS, Nor RM (2015) Evaluation of Williamson???hall strain and stress distribution in ZnO nanowires prepared using aliphatic alcohol. J Nondestruct Eval 34:1–9. https://doi.org/10.1007/s10921-015-0286-8

37. Xiong HM, Zhao X, Chen JS (2001) New polymer-inorganic nanocomposites: PEO-ZnO and PEO-ZnO-LiClO4films. J Phys Chem B 105:10169–10174. https://doi.org/10.1021/jp0103169

38. Quality HP, Berkeley L (2018) Lawrence Berkeley National Laboratory Lawrence Berkeley National Laboratory, Lawrence Berkeley. Natl Lab 12. https://doi.org/10.1007/978-3-319-46448-0

39. Berzina-Cimdina L, Borodajenko N (2012) Research of calcium phosphates using fourier transform infrared spectroscopy. Infrared Spectrosc Mater Sci Eng Technol. https://doi.org/10.5772/36942

40. Martinez CR, Joshi P, Vera JL, Ramirez-Vick JE, Perales O, Singh SP (2011) Cytotoxic studies of PEG functionalized ZnO nanoparticles on MCF-7 cancer cells. NSTI Nanotechnol Conf Expo 3:420–423

41. Srikant V, Clarke DR (1998) On the optical band gap of zinc oxide. J Appl Phys 83:5447–5451. https://doi.org/10.1063/1.367375

42. Jain N, Bhargava A, Panwar J (2014) Enhanced photocatalytic degradation of methylene blue using biologically synthesized "protein-capped" ZnO nanoparticles. Chem Eng J 243:549–555. https://doi.org/10.1016/j.cej.2013.11.085

43. Khorsand Zak A, Razali R, Abd Majid WH, Darroudi M (2011) Synthesis and characterization of a narrow size distribution of zinc oxide nanoparticles. Int J Nanomedicine 6:1399–1403. https://doi.org/10.2147/ijn.s19693

44. Wu L, Wu Y, Lü W (2005) Preparation of ZnO nanorods and optical characterizations. Phys E Low-Dimensional Syst Nanost 28:76–82. https://doi.org/10.1016/j.physe.2005.02.005

45. Anandan M, Dinesh S, Krishnakumar N, Balamurugan K (2017) Tuning the crystalline size of template free hexagonal ZnO nanoparticles via precipitation synthesis towards enhanced photocatalytic performance. J Mater Sci Mater Electron 28:2574–2585. https://doi.org/10.1007/s10854-016-5833-2

46. Pradhan D, Mohapatra SK, Tymen S, Misra M, Leung KT (2011) Morphology-controlled ZnO nanomaterials for enhanced photoelectrochemical performance. Mater Express 1:59–67. https://doi.org/10.1166/mex.2011.1008

47. Chen C, Li X, Ma W, Zhao J, Serpone N (2002) Effect of transition metal ions on the TiO2—assisted Photodegradation of dyes under visible irradiation : a probe for the interfacial electron transfer process and reaction mechanism. J Phys Chem B 106:318–324. https://doi.org/10.1021/jp0119025

48. Studenikin SA, Golego N, Cocivera M (1998) Fabrication of green and orange photoluminescent, undoped ZnO films using spray pyrolysis. J Appl Phys 84:2287–2294. https://doi.org/10.1063/1.368295

49. Rajkumar C, Arulraj A (2018) Seed mediated synthesis of nano-sized zinc oxide and its electron transporting activity in dye-sensitized solar cells. Mater Res Express 5:15029. https://doi.org/10.1088/2053-1591/aaa2b3

50. Devi PG, Velu AS (2016) Synthesis, structural and optical properties of pure ZnO and Co doped ZnO nanoparticles prepared by the co-precipitation method. J Theor Appl Phys 10:233–240. https://doi.org/10.1007/s40094-016-0221-0

51. Biroju RK, Giri PK (2017) Strong visible and near infrared photo-luminescence from ZnO nanorods/nanowires grown on single layer graphene studied using sub-band gap excitation. J Appl Phys 122:15–20. https://doi.org/10.1063/1.4995957

52. Fan XM, Lian JS, Zhao L, Liu YH (2005) Single violet lumines-cence emitted from ZnO films obtained by oxidation of Zn film on quartz glass. Appl Surf Sci 252:420–424. https://doi.org/10.1016/j.apsusc.2005.01.018

53. Bhattacharyya S, Gedanken A (2008) Microwave-assisted inser-tion of silver nanoparticles into 3-D mesoporous zinc oxide nanocomposites and nanorods. J Phys Chem C 112:659–665. https://doi.org/10.1021/jp0760253

54. Kumar Jangir L, Kumari Y, Kumar A, Kumar M, Awasthi K (2017) Investigation of luminescence and structural properties of ZnO nanoparticles, synthesized with different precursors. Mater Chem Front 1:1413–1421. https://doi.org/10.1039/c7qm00058h

55. Shen Z, Zhou H, Chen H, Xu H, Feng C, Zhou X (2018) Synthesis of nano-zinc oxide loaded on mesoporous silica by coordination effect and its photocatalytic degradation property of methyl orange. Nanomaterials 8:317. https://doi.org/10.3390/nano8050317

56. Wang Z, Wang K, Wang H, Chen X (2018) Catalysis science & technology the correlation between surface defects and the. Catal Sci Technol 10:15–20. https://doi.org/10.1039/c8cy00550h

57. Iaiche S, Djelloul A (2015) ZnO/ZnAl2O4 nanocomposite films studied by X-ray diffraction, FTIR, and X-ray photoelectron spec-troscopy. J Spectrosc. https://doi.org/10.1155/2015/836859

58. Neena D, Kondamareddy KK, Bin H, Lu D, Kumar P (2018) Enhanced visible light photodegradation activity of RhB / MB from aqueous solution using nanosized novel Fe–Cd co-modi-fied ZnO. Sci Rep. https://doi.org/10.1038/s41598-018-29025-1

59. Kayaci F, Vempati S, Ozgit-Akgun C, Biyikli N, Uyar T (2014) Enhanced photocatalytic activity of homoassembled ZnO nano-structures on electrospun polymeric nanofibers: a combination of atomic layer deposition and hydrothermal growth. Appl Catal B Environ 156–157:173–183. https://doi.org/10.1016/j.apcatb.2014.03.004

60. Alshammari AS, Chi L, Chen X, Bagabas A, Kramer D, Alromaeh A, Jiang Z (2015) Visible-light photocatalysis on C-doped ZnO derived from polymer-assisted pyrolysis. RSC Adv 5:27690–27698. https://doi.org/10.1039/c4ra17227b

61. Cherrad H, Bahedi K (2016) Strain effect on the green and red emissions of Zno: Zr thin films deposited by spray pyrolysis. Int J Adv Inf Sci Technol 44:83–87

62. Woo J-C, Kim C-I (2010) The dry etching properties of ZnO thin film in Cl$_2$/BCl$_3$/Ar plasma. Trans Electr Electron Mater 11:116–119. https://doi.org/10.4313/TEEM.2010.11.3.116

63. Rodriguez BJ, Shields BJ, Nemanich RJ (2004) ZnO {0001} surfaces n-type, ZnO 0001‰ surfaces. https://doi.org/10.1063/1.1695596

64. Kurisu S, Iwasaki T, Ishibashi K, Mitsuba N, Dohi Y, Kihara Y (2013) Comparison of treatment and outcome of acute myocardial infarction between cancer patients and non-cancer patients. Int J Cardiol 167:2335–2337. https://doi.org/10.1016/j.ijcard.2012.11.009

65. Akir S, Barras A, Coffinier Y, Bououdina M, Boukherroub R, Omrani AD (2016) Eco-friendly synthesis of ZnO nanoparti-cles with different morphologies and their visible light pho-tocatalytic performance for the degradation of Rhodamine B. Ceram Int 42:10259–10265. https://doi.org/10.1016/j.ceramint.2016.03.153

66. Júnior EAA, Nobre FX, da Silva Sousa G, Cavalcante LS, Santos MRDMC, Souza FL, de Matos JME (2017) Synthesis, growth mechanism, optical properties and catalytic activity of ZnO microcrystals obtained via hydrothermal processing. RSC Adv 7:24263–24281. https://doi.org/10.1039/c7ra03277c

67. Kumar SG, Rao KSRK (2015) Zinc oxide based photocatalysis: tailoring surface-bulk structure and related interfacial charge carrier dynamics for better environmental applications. RSC Adv. 5:3306–3351. https://doi.org/10.1039/c4ra13299h

68. Cabansag JLJ, Dumelod JC, Alfaro JCO, Arsenal JD, Sambot JC, Enerva LT, Leaño JL Jr (2013) Photocatalytic degradation of aqueous CI reactive violet 5 using bulk zinc oxide (ZnO) slurry. Philip J Sci 142(1):77–85

69. Eswar NKR, Ramamurthy PC, Madras G (2016) Novel syner-gistic photocatalytic degradation of antibiotics and bacteria using V–N doped TiO$_2$ under visible light: the state of nitro-gen in V-doped TiO$_2$. New J Chem 40:3464–3475. https://doi.org/10.1039/c5nj02861b

70. Pelaez M, Falaras P, Likodimos V, O'Shea K, de la Cruz AA, Dunlop PSM, Byrne JA, Dionysiou DD (2016) Use of selected scavengers for the determination of NF-TiO$_2$ reactive oxygen species during the degradation of microcystin-LR under visible light irradiation. J Mol Catal A: Chem 425:183–189. https://doi.org/10.1016/j.molcata.2016.09.035

71. Talukdar S, Dutta RK (2016) A mechanistic approach for super-oxide radicals and singlet oxygen mediated enhanced photo-catalytic dye degradation by selenium doped ZnS nanoparticles. RSC Adv 6:928–936. https://doi.org/10.1039/c5ra17940h

72. Fatimah I (2018) Advance oxidation treatment of dye waste using ZnO/activated carbon under UV illumination. p 020004. https://doi.org/10.1063/1.5064964

73. Rahman QI, Ahmad M, Misra SK, Lohani M (2013) Effective pho-tocatalytic degradation of rhodamine B dye by ZnO nanopar-ticles. Mater Lett 91:170–174. https://doi.org/10.1016/j.matlet.2012.09.044